

Equatorial F -region plasma drifts: A study using OI 630 nm emission all-sky images

M. Hari Kishore¹ and G. K. Mukherjee^{2,*}

¹Department of Physics, Andhra University, Visakhapatnam 500 003, India

²Indian Institute of Geomagnetism, New Panvel (W), Navi Mumbai 410 218, India

The equatorial ionospheric plasma bubbles that occur at the low-latitude F -region of the ionosphere and the irregularities associated with them are responsible for severe interference and sudden disruption of trans-ionospheric radio propagation up to Giga Hertz frequency range, interfering with the communication systems, including the GPS. A CCD-based all-sky imager with 180° field-of-view has been operating at a low-latitude station, Kolhapur (16.8°N , 74.2°E , dip lat. 10.6°N) in India on clear, moonless nights, to study the F -region dynamics through the imaging of OI 630.0 nm oxygen emission line. The imager has the capability of permitting observations over regions covering several million square kilometres from a single observing station. The ionospheric plasma bubbles manifest in all-sky imaging observations as nearly north–south aligned intensity-depleted regions. The all-sky images permitted the determination of the eastward plasma drift velocities, depth and width of the plasma bubbles. Also, the observed zonal plasma bubble drift velocities are compared with the thermospheric zonal neutral wind velocities obtained from the HWM-93 model. It reveals good agreement during some nights. The rate of change of zonal wind velocities has been modelled and is found to be consistent in terms of pressure variation computed from the MSIS-E 90 model.

Keywords: All-sky imager, equatorial plasma bubbles, F -region, nightglow, oxygen emission line.

IONOSPHERIC plasma irregularities associated with night-time equatorial spread- F phenomena¹ have been the subject of intensive experimental and theoretical investigations during recent times. These irregularities have been observed using ionosondes^{2–6}, topside sounders^{7–9}, and *in situ* rocket and satellite^{10–12} measurements as well as optical techniques (conventional tilting and scanning photometers and wide-angle optical imaging system)^{11–15}. The continuing interest in studies related to the equatorial spread- F irregularities increased from its implications for trans-ionospheric communications and navigation systems.

The scale size of the irregularities varies between tens of centimetres to hundreds of kilometres, which are sensitive to a wide range of diagnostic techniques⁴. Several re-

searchers have used wide-angle imaging of the F -region night-glow emissions to study large-scale plasma irregularities^{11–16}. The irregularities characterized by large-scale ionospheric plasma depletions are generally called plasma bubbles. These are the regions where the plasma densities decrease abruptly by several orders of magnitude compared to the ambient plasma densities. The HF communications and satellite-to-ground communication navigation based on satellites such as GPS get affected by these plasma irregularities. Weber *et al.*¹⁵ observed the first magnetically N–S aligned structures of low-intensity OI 630.0 nm air-glow images during the period of spread- F observations. These low-intensity regions are the optical signatures of depletions, which are mapped in the all-sky images of OI 630.0, 557.7 and 777.4 nm emissions. According to the present theoretical interpretations, large-scale plasma depletions or spread- F bubbles are initially generated at the F -region bottom side, through a fluid-type gradient instability mechanism, such as the gravitational Rayleigh–Taylor instability^{17–19} in conjunction with $E \times B$ instability²⁰ with seeding perturbations provided by gravity waves, vertical winds and electric fields^{13–16,21,22}. Evidence from backscatter radar²³ shows that quasi-periodic ‘bubbles’ or ‘equatorial spread- F ’ (ESF) could be ‘seeded’ by gravity waves having horizontal wavelengths of the order of 100 km at altitudes of around 200 km (the bottom of the F -layer).

The ionospheric plasma bubbles (depletions) are generally aligned along the magnetic field lines, owing to the much greater conductivity in the magnetic field direction compared with the perpendicular conductivity. As these bubbles move buoyantly upward with respect to the ambient plasma in the equatorial region, their bottom side feet migrates away from the equator, reaching dip latitudes²⁴ of over $\pm 15^\circ$. At the boundaries and within the bubbles, small-scale size irregularities are generally produced which give rise to strong VHF night-time scintillations in the satellite beacon signals. The plasma drift velocities associated with the bubbles constitute an important parameter for thermospheric studies. These bubbles usually drift eastward in the equatorial ionosphere and are often tilted to the west of the magnetic meridian because of the upward motion of the bubble. The use of all-sky optical imaging systems has been especially important in studying the spatial extent of the bubbles and their motion relative to the surrounding ambient ionosphere^{25–27}. A charge cou-

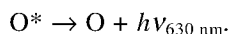
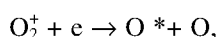
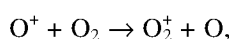
*For correspondence. (e-mail: gkm@iigs.iigm.res.in)

pled device (CCD)-based all-sky imaging system (180° field-of-view) developed in collaboration with Boston University, USA, was operated from Kolhapur on clear, moonless nights, to obtain the signatures of the dynamics of the plasma bubbles by studying the images at OI 630.0, 557.7 and 777.4 nm. Data for the generation and evolution of these large-scale irregularities are limited at the Indian longitude sector²⁵. The location of the observing station is important, as a single image frame at a given instant provides information regarding the dynamics of these over a large, low-latitude region, starting from the geomagnetic equator to the equatorial ionospheric anomaly region.

Here we present and discuss some of the results of the ionospheric plasma bubble zonal drifts from the OI 630.0 nm all-sky imaging observations carried out during the period March 1998 to March 2001 at Kolhapur and Panhala (17.0°N, 74.2°E). The significant features of the ionospheric plasma bubble zonal drift velocities, inferred from the all-sky imaging measurements are analysed. A comparison of the observed ionospheric plasma bubble zonal drifts with eastward component of *F*-region neutral wind from HWM93 model has also been investigated.

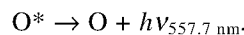
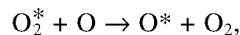
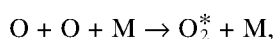
Tropical atomic oxygen night-glow emission mechanism

The OI 630.0 nm night-glow emission comes from a narrow layer concentrated near 300 km altitude in the bottom side of the *F*-layer and is an optical manifestation of several ionospheric processes¹¹. The peak heights of the emission layer vary between 230 and 270 km. At the equator and low-latitudes the OI 630.0 nm emission is mainly due to dissociative recombination of O⁺ ions in the *F*-region, produced by a two-step process.



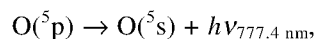
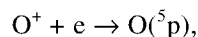
It is understood that this emission is strongly dependent on the height changes associated with the bottom side of the *F*-region, with smaller dependence to the changes in the *F*-region electron density. The spatial distribution is mostly governed by the EXB vertical plasma drifts and thermospheric neutral winds.

On the other hand, a major portion of the OI 557.7 nm emission comes from the recombination of atomic oxygen atoms in the mesopause region (80–100 km). The OI 557.7 nm emission is excited by the two step energy transfer process:



A fraction of these emissions also originates from the dissociative recombination of atomic oxygen atoms in the *F*-region. It is estimated to be about 20% of the *F*-region OI 630.0 nm contribution¹¹.

The OI 777.4 nm emission is produced mainly by the radiative recombination process



and it provides an indirect measurement of the *F*-region peak electron density $n_m(e)$. The OI 777.4 nm emission observed at Kolhapur during the present study has been low, they have not been included in our studies.

Instrumentation

All-sky camera

A CCD-based all-sky imaging system (Figure 1) has a fish-eye lens (16 mm, *f*/2.8) at the top of the camera, which takes in light in 2π steradians from the sky. The function of the 40 mm diameter field lens and the 300 mm, *f*/2.5 Aero Ektar lens is to collimate light from the sky. The fish-eye lens produces a circular image of the sky 23 mm in diameter, which is directed into the collimator. Finally after passing through the filter the light is re-imaged at *f*/1 onto the photo-cathode of the intensified CCD of a Fairchild model 3000 and intensifier type 4727 of ITT. The detector is housed in a chamber which is thermoelectrically cooled to 60°C below ambient temperature to re-

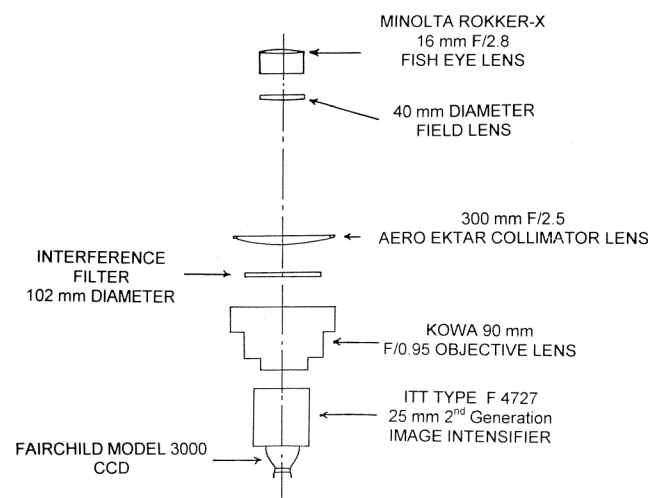


Figure 1. Schematic of the all-sky imager.

duce the dark signal. Very weak night-glow signals can be monitored with the system with large integration time. There are six filter positions, which can be used to study various emission lines originating at different ionospheric and thermospheric heights. Since our main concern is to study the *F*-region dynamics at night, we concentrate on spatial and temporal characteristics of the OI 630.0 nm emission.

Geometry of observations

Figure 2 shows the location of the observing station, Kolhapur with respect to geographic coordinates. The two circles indicate the coverage of the imaging system for zenith distances 75° and 90° for an emission height of 300 km.

Figure 3a shows the 75° zenith angle distance of 300 km height, which encompasses approximately 8° of latitude/longitude from the zenith; this is equivalent to a horizontal diameter of ~1800 km through the zenith at 300 km. Between zenith angles 75° and 90°, an additional 8° latitude/longitude is encompassed.

Due to compression effects these regions are not accurate for image analysis. It is important to note, however, that the geomagnetic equator falls within 75–90° zenith angles and appears near the southern edge of the field-of-view. Figure 3b shows the image overlay pattern as seen from Kolhapur. The north–south aligned motions of the bubbles can be used to find the bubble altitude above the magnetic equator by tracing the magnetic field line at a given point assuming that the emitting layer is situated at 300 km altitude. A depleted region reaching the extreme northern edge of the image (Figure 3b) will correspond to an altitude greater than 1500 km above the equator.

Observations

The wide-angle imaging technique offers the unique capability to characterize simultaneously the morphology of

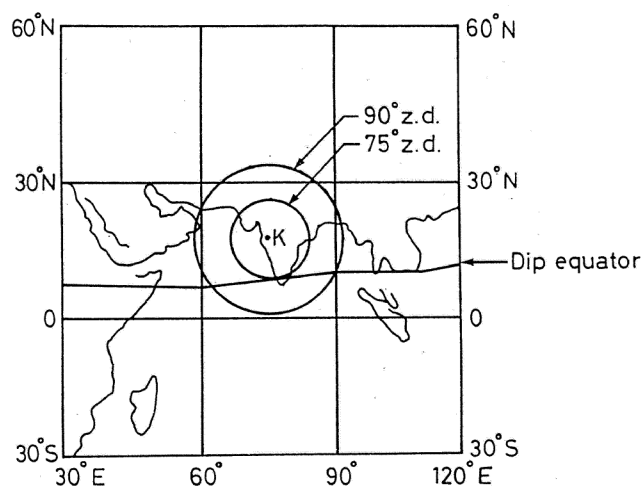


Figure 2. Field-of-view at 75° and 90° zenith angles at 300 km for the all-sky imager at Kolhapur.

plasma-depleted flux tubes over a large geographical area. For the present investigation, we have studied the all-sky images that obtained from the all-sky imager located at Kolhapur during the high solar activity period, March 1998 to March 2001, in order to investigate the nocturnal behaviour of the ionospheric plasma bubble zonal drifts in the equatorial and low-latitude regions on clear, moonless nights. We have used the all-sky images of OI 630.0 nm emission for several nights; the list is shown in Table 1. The decimetric solar flux indices ($F_{10.7}$ cm) for all the days of our observations varied between (units of 10^{-22} Wbm $^{-2}$) 100 and 229. The magnetic activity K_p indices during the period of observation were between 1 and 5. All-sky images were captured with OI 630.0 nm filter with a narrow bandwidth (1 nm) after few minutes interval. Time was expressed in IST (Indian Standard Time), which is ahead of UT by five and a half hours. The fish-eye lens image has been converted into an image in geographic coordinates by assuming an emission height of 300 km for the OI 630.0 nm emission. The mean image was obtained by averaging together a series of images (in 1 h) processed using IDL software. The mean image obtained was used to flat field the image dataset. The non-uniformity of the image due to van Rhijn effect, atmospheric extinction and non-uniform sensitivity of the imager is roughly corrected by this process.

Observations on 1 March 2000: In Figure 4, we show the processed images of OI 630.0 nm for the night of 1 March 2000 at 22:06, 22:12, 22:16, 22:21, 22:35, 22:45 h IST. Dark regions represent low airglow-intensity and were thus associated regions where electron density was depleted relative to the background. The quasi north-south magnetic field-aligned depletions (dark structures) seen in the images were optical signatures of the plasma bubbles.

At 22:06 IST the image shows two prominent depletions. The strength of the depletions starts decreasing from 22:21 IST onwards, while moving towards east.

Table 1 shows the results of twelve nights of our observation. Simultaneous depletions in other *F*-region oxygen emission lines were also noted on ten nights. The simultaneous depletions in OI 630.0, 557.7 and 777.4 nm emissions on the night of 2 March 2000 at 23:24 to 23:44 IST are shown in Figure 5. The amplitude of the intensity of depletion was larger for OI 630.0 nm than OI 557.7 nm line. This might be due to the relative intensity and the difference in life time between the OI (1D) and O (1S) states, which are responsible for the OI 630.0 and 557.7 nm emissions. The overall intensity of the OI 777.4 nm emission is less than the OI 630.0 nm emission. The images show more or less similar structures of depletion. The altitude–latitudinal extent of the intensity-depleted regions can be mapped along the magnetic field lines to equatorial crossing altitudes using Figure 3b. It can be inferred from the all-sky images in Figures 4 and 5 that the corresponding plasma-depleted flux tube crosses

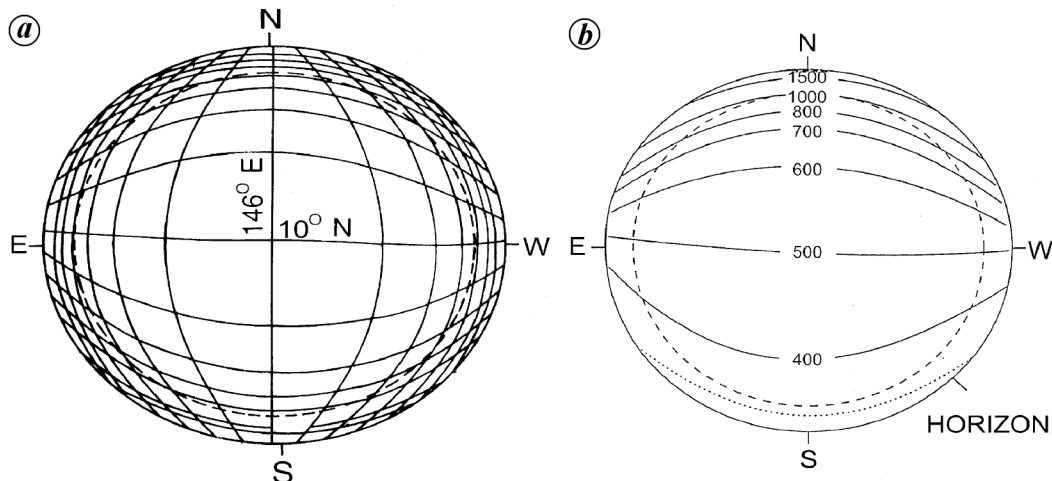


Figure 3. *a*, Dip latitudes and magnetic longitudes of geomagnetic field lines at 2° intervals observed at 300 km altitude at Kolhapur. *b*, Projected altitude over the equator for OI 630 nm emission at 300 km for Kolhapur situated at the centre. Dotted line represents the magnetic equator, dashed line represents a 75° zenith distance.

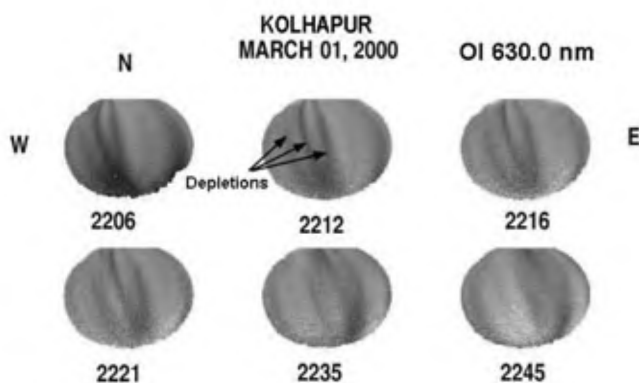


Figure 4. All-sky images of OI 630.0 nm emission on the night of 1 March 2000 at Kolhapur showing several depletion regions moving towards east with westward tilt.

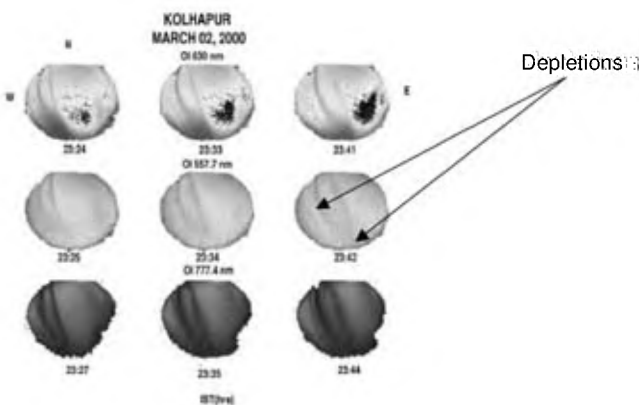


Figure 5. Simultaneous depletions observed in OI 557.7, OI 630.0 and OI 777.4 nm images on the night of 2 March 2000 at Kolhapur.

the magnetic equatorial plane at an altitude above 1500 km.

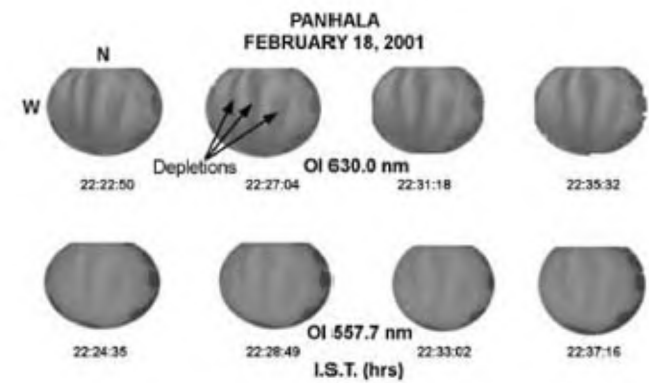


Figure 6. Depletions observed in OI 630.0 nm images on the night of 18 February 2001.

Observations on 18 February 2001: Figure 6 shows another example of simultaneous depletions observed in both OI 630.0 and OI 557.7 nm emissions on the night of 18 February 2001 at Panhala during 22:22:50–22:37:16 IST. In order to compute the drift velocity of the plasma bubbles we scanned several images from east to west (through the zenith) after flat-fielding them and calculated OI 630.0 intensity at each pixel. Figure 7 shows the OI 630.0 nm images observed at Panhala on the night of 18 February 2001 between 21:15:09 and 22:35:32 IST. The images show north-south aligned plasma depletions with varying depths and widths. Most of the bubbles were well developed and reached heights of about 1500 km at the equatorial altitude.

Width and depth of depletions

In order to find the depth and width of the depletions, we scanned several images from east to west (through zenith)

Table 1. Comparison between observed zonal plasma drifts and computed velocity of zonal component of neutral wind using the HWM 93 model

Period	Time (IST)	Station	K_p	$F 10.7 \text{ cm}$	Drift velocity (m/s)	Neutral wind (zonal component) velocity HWM model (m/s)
25 and 26 March 1998	2100	Kolhapur	5–	114	124	136
	2200				121	114
	2300				55	84
	0000				25	56
	0100				–	33
14 and 15 March 1999	2100	Kolhapur	3_0	149	134	158
	2200				122	138
	2300				110	109
	0000				112	79
	0100				76	54
14 and 15 April 1999	2100	Kolhapur	2–	121	163	146
	2200				125	124
	2300				105	95
	0000				103	68
1 and 2 March 2000	2100	Kolhapur	3+	227	197	162
	2200				192	143
	2300				190	114
	0000				126	84
	0100				82	59
2 and 3 March 2000	2200	Kolhapur	1–	210	251	151
	2300				148	123
	0200				67	54
	0300				41	40
3 and 4 March 2000	2200	Kolhapur	1+	204	228	156
	2300				208	129
	0000				163	102
	0001				130	80
	0002				120	63
5 and 6 March 2000	2100	Kolhapur	2–	217	207	173
	2200				180	155
	2300				144	128
	0000				–	100
	0100				–	77
22 and 23 January 2001	2100	Panhala	3–	157	206	161
	2200				137	148
	2300				85	128
	0000				109	108
	0100				170	93
25 and 26 January 2001	2100	Panhala	2–	163	262	167
	2200				197	154
	2300				146	134
	0000				163	115
	0100				119	100
18–19 February 2001	2100	Panhala	1–	129	132	175
	2200				162	160
	2300				169	136
	0100				110	92
19 and 20 February 2001	2100	Panhala	1_0	134	201	174
	2200				147	159
	2300				139	134
	0000				80	105
26 and 27 March 2001	2100	Kolhapur	1–	267	262	172
	2200				112	153
	2300				115	124
	0000				150	95
	0100				–	71

after flat-fielding them and calculated OI 630.0 nm intensity at each pixel (east–west) using the IDL software. Figure 8 gives an example of the plot of the OI 630.0 nm intensity variation as a function of pixel number (E–W) for 25 March 1998 at Kolhapur during the period 23:00–23:24 IST. We studied how the size (east–west width in kilometres) of the bubbles and depth (difference between maxima and minima in intensity values as a percentage of maximum) of depletion observed at Kolhapur fluctuated with the evolution of time. Figure 9 shows the degree of depletion as a function of width of the depletion for two nights at three different hours. The degree of depletion observed for the period of observation varied between 12 and 25% with corresponding width of the bubble ranging from 75 to 130 km. A straight-line fit to all the data-points showed that the degree of depletion varied



Figure 7. OI 630.0 nm images observed at Panhala on the night of 18 February 2001 showing north–south aligned plasma bubbles.

linearly with the width of the plasma bubble. Thus regions having high degree of depletion were observed to be associated with larger depletions compared to shallower depletions. This appears to be the manifestation of the fact that deeper depletions are characterized by large amplitudes and represent well-developed irregularities, while shallower depletions depict weaker irregularities, which are in their formative stages.

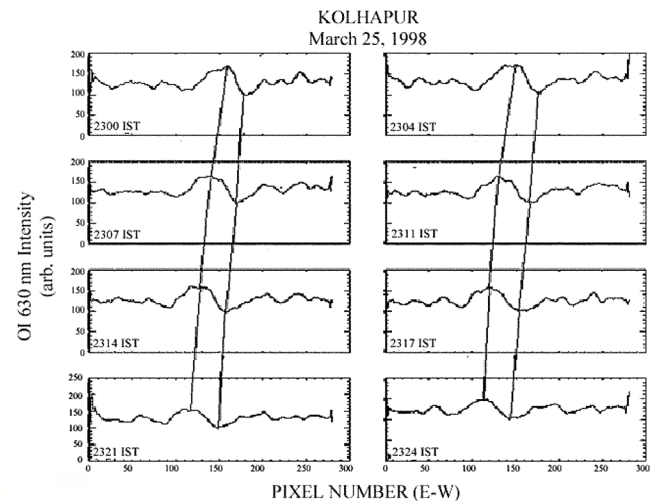


Figure 8. Intensity plot of OI 630.0 nm showing movement of ionospheric plasma depletions at 23:00–23:24 h IST on the night of 25 March 1998 as a function pixel number in the east–west direction at Kolhapur.

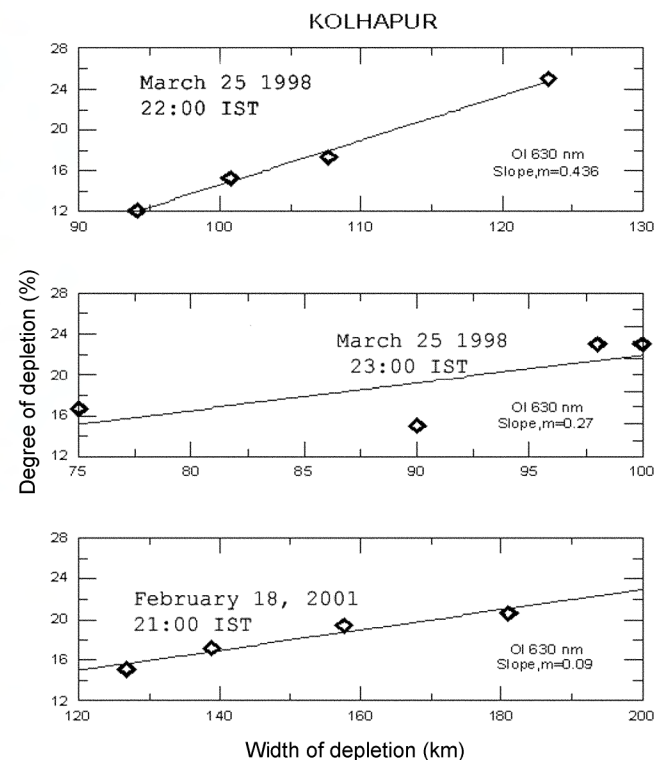


Figure 9. Variation in the degree of depletion with width (east–west extent) of plasma depletions observed in 630 nm images on 25 March 1998 and 18 February 2001. Slope of the straight line m is also shown.

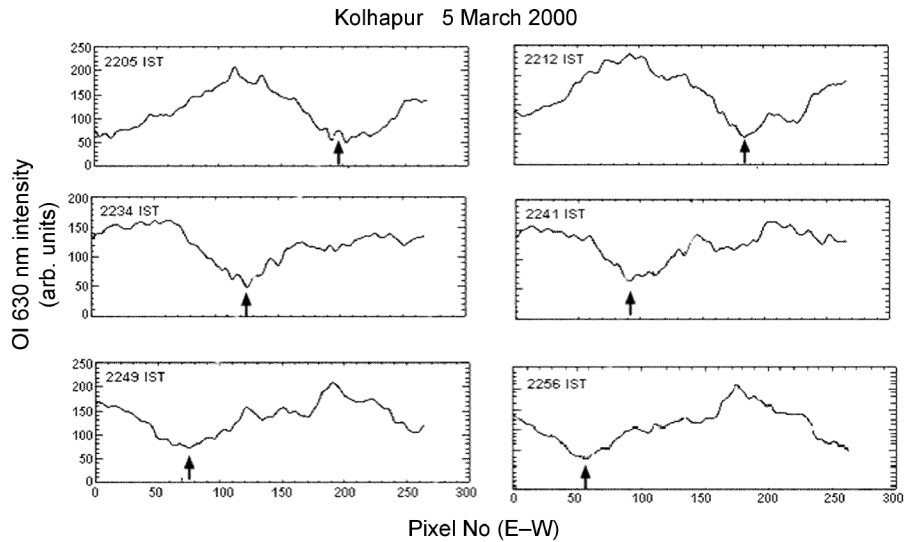


Figure 10. Intensity plot of OI 630.0 nm showing the width and depth of ionospheric plasma depletions at 22:05–22:56 IST on the night of 5 March 2000, as a function of pixel number in the east–west direction at Kolhapur.

Table 2. The inter-depletion distances for plasma depletions observed in OI 630.0 nm on 18 February 2001 at Panhala

Date	Emission	Time (IST)	IDD (km)
18 February 2001	OI 630 nm	2218	244
		2222	248
		2227	257
		2231	238
		2235	262
		2239	260
		2244	236
		2248	266

Similarly we also computed the inter depletion distances (IDD) between adjacent depletions using OI 630.0 nm images on the night of 18 February 2001 at Panhala. Results are shown in Table 2. The distances of separation varied between 236 and 266 km. This is of the order of the horizontal wavelength of the gravity waves which are the sources of perturbation at the base of the *F*-region during spread- $F^{18,28,29}$.

Comparison of observed plasma drift velocities with HWM model

From the spatial displacements of the irregularity structures of the depletions observed in successive images, we can infer the zonal component of the drift velocities of the depletions which are closely related to the ionospheric plasma zonal drift velocities at night. Also at night-time, ionospheric plasma drift velocities in the equatorial and low-latitude regions are approximately equal to the thermospheric zonal wind³⁰. By comparing successive images, the speed and direction of the airglow features

(bubbles) were measured as a function of local time. Figure 10 shows the OI 630.0 nm intensity plot of images as a function of pixel number in the east–west direction on the night of 5 March 2000. It shows the movement of the bubbles marked by arrows in eastward direction. The western wall of the bubbles depicts more wavy structures. Also, the high intensity regions move with the bubbles almost with the same speed. From the two successive plots we can measure the number of pixels or spatial distance covered by the depletion (bubble) while moving towards the east. Using the conversion of transforming the image into geographical coordinates, it is possible to change the pixel number into zenith angle³¹. From the change in zenith angle we can measure the zenith distance that is travelled by the bubble in a given period. The results are shown in Table 1 along with the parameters of solar flux *F* 10.7 cm and magnetic indices *K_p* for the given days. On an average, the observed drift speeds range between 50 and 260 m/s. In general the observed drift speeds reach maximum value during 21:00–23:00 h IST.

In the absence of zonal *F*-region wind measurements, we compared the observed plasma drift velocities with the zonal component of neutral wind velocity computed using Hedin’s empirical HWM 93 model³² during the period of observation. We have used this model to see if it adequately reproduces the zonal ionospheric plasma bubble drift velocities at low latitude. This model is an extended version of the HWM 90 model with variations in magnetic activity (*A_p*) included. Mid- and low-latitude data were reproduced quite well by the model. The model describes the transition from predominantly diurnal variations in the upper thermosphere to semidiurnal variations in the lower thermosphere and a transition from summer

to winter flow above 140 km, to winter to summer flow below 140 km. Significant altitude gradients in the wind extended up to 300 km at some local times. This model provides comprehensive statistical estimates based entirely on observational data. Inputs to the model include day of the year, local time, latitude, longitude, altitude, solar flux ($F_{10.7}$ cm) and geomagnetic activity (A_p). The model software provides zonal and meridional winds for specified latitude, longitude, time and A_p index. Nocturnal variations of the zonal component of wind velocity computed from the model are depicted in Table 1 for the twelve selected nights.

In Figure 11 *a*, we plot the zonal component of the neutral wind velocities as a function of local time (IST) computed using this HWM 93 model for 14 March 1999 at Kolhapur. The observed plasma drifts computed from the images of OI 630.0 nm have been compared with the zonal component of neutral wind velocities computed from the HWM 93 model (Figure 11 *a*). The plasma drifts were 134, 122, 110, 112 and 76 m/s at 21:00, 22:00, 23:00, 00:00, 01:00 LT respectively. For the same period using the HWM model the calculated neutral wind velocities were 158, 138, 109, 79 and 54 m/s. Although there were differences in the magnitudes, the two sets of values showed a similar trend. Similarly, wind velocities computed using the HWM 93 model are also shown for 1–2 March 2000 (Figure 11 *b*). The observed *F*-region drifts were higher than the model-predicted values by 20% during 21:00–23:00 h IST and the differences were reduced as the night progressed. The agreement between the two sets of values was better on the nights of 25–26 March 1998 and 14 and 15 March 1999. The differences between the observed drifts and the zonal component of neutral winds could be explained due to the uncertainties in the assumed height of the emission layer during the period of observation. Also, on an average, the drift speeds decreased steadily reaching their minimum value during post-midnight hours. The model also compared well with the equatorial zonal neutral wind flow measurements using WATS (Wind and Temperature Spectrometer) aboard DE-2 satellite in 1981, as well as ground-based zonal ion drift measurements using the Jacamarca incoherent radar for the corresponding period¹⁷.

Thus, this comparison of the zonal plasma drift speed with theoretical zonal neutral wind velocity measurements using the HWM 93 model showed that the night-time zonal component of the neutral wind and the ambient plasma moved in the same direction with nearly equal velocities¹². This also provides evidence that the *F*-region neutral winds were the source of the electric fields driving ion drifts in the tropical latitudes.

Zonal wind (plasma drift)

Zonal wind is responsible for the pre-reversal enhancements in the evening vertical ionization drift as well as

the night-time zonal plasma drift driven by the downward polarization electric field that it produces under the decay of the *E*-layer conductivity. Depending on the ratio of the field line-integrated conductivity of the *F*-layer to that of the conjugate *E*-layers, a given constant zonal wind can produce a height-varying zonal plasma drift near the F2 peak in such a way that the zonal plasma drift near the F2 peak often represents a good measure of the thermospheric zonal wind for the same height region.

Near the geomagnetic equator, the ions and electrons in the *F*-region can drift in response to dynamo electric fields induced by the neutrals. This dynamo or polarization electric field is established by the motion of the neutrals across the magnetic field lines, which impart their motion to the electrons and ions initially in the same direction. The electrons then separate from the ions producing polarization charge responsible for the dynamo field. The field in turn accelerates the ions in the same direction as neutrals, reducing the effective ion-drag. If none of the polarization charge is drained away, the field may be strong enough to make the ion drift as large as the zonal neutral wind.

It has been found that the ratio of the zonal ion drift to the zonal neutral wind should be significantly smaller than 1.0 in the daytime and closer to 1.0 at night. During daytime the polarization charge is drained effectively by the highly conductive daytime *E*-region at lower altitudes and

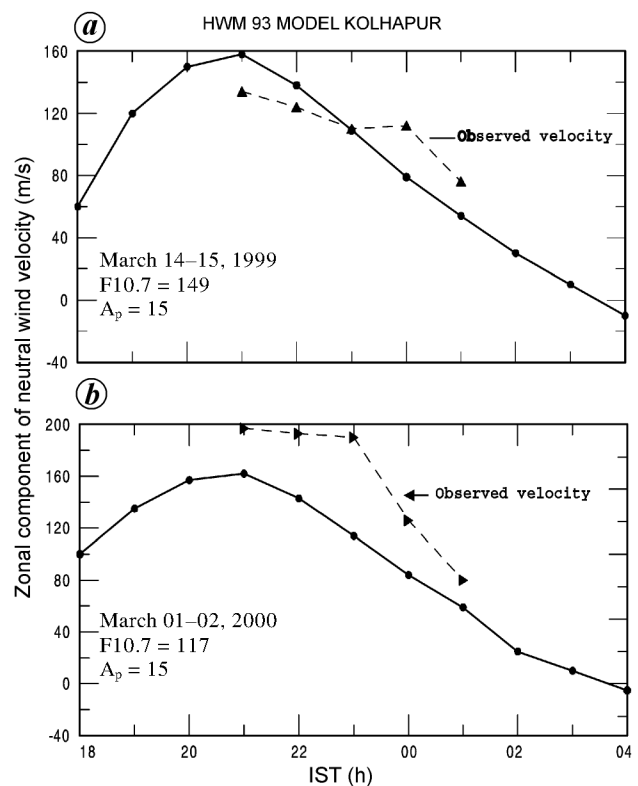


Figure 11. Comparison of zonal component of neutral wind velocity computed from Hedin's model (HWM 93) and eastward component of observed velocity of depletions (OI 630.0 nm) from all-sky images on (a) 14 and 15 March 1999 and (b) 1 and 2 March 2000 at Kolhapur.

at latitudes away from the equator. At night, when the E -region disappears, the polarization charge is not drained away, and a significant polarization field is developed.

The zonal wind in the tropical region is driven locally by the zonal component of the pressure gradient, and moderated by ion drag and viscosity. After neglecting the Coriolis force and gravity the equation of motion of the neutral wind in the x (zonal) direction is

$$\frac{\partial U_x}{\partial t} = -\frac{1}{\rho} \frac{\partial P}{\partial x} + \frac{\mu}{\rho} \frac{\partial^2 U_x}{\partial Z^2} - v_{ni}(U_x - V_{ix}),$$

where v_{ni} is the ion neutral collision frequency, V_{ix} the zonal ion drift, μ is the viscosity coefficient and ρ the mass density. In the zonal wind term, the pressure gradient term $(1/\rho)(\partial P/\partial x)$ is computed by variations in temperature and density for an altitude of 300 km obtained using the MSIS-E 90 model³³. In this term, if longitude and local time variations are assumed to be equivalent, $\partial/\partial x$ can be replaced by a time derivative $(\Omega R \cos \phi)^{-1} \partial/\partial t$ (except at the poles), where Ω , R and ϕ are the earth's angular velocity, radius and geographic latitude respectively²⁶. During the night the ionospheric plasma bubble drifts and the night-time zonal wind speeds are assumed to be nearly equal. So, the third term in the zonal wind balance equation is almost equal to zero. The viscosity term is not estimated here, since we have no observations of the vertical wind

distribution. The ion-drag term is negligibly small, not sufficiently strong to counteract the pressure gradient term. Variations of different terms in the equation of motion are shown in Figure 12 for 1 March 2000 at Kolhapur. Thus in region I, $\partial P/\partial x$ is large, probably producing the large $\partial U_x/\partial t$ observed in Figure 11b, from 20:00 to 21:00 h IST. In region II, the ion-drag term is sufficiently strong to counteract the pressure gradient term. Thus $\partial U_x/\partial t$ is reduced in this region due to the ion-drag term. In the regions III and IV again the pressure gradient term decreases. This explains the observed computed zonal wind enhancement in the period between 18:00 IST to 21:00 h IST. Thus, the zonal component of the neutral wind is mainly dependent on the pressure gradient term.

Thus the roles played by the different terms in the momentum equation above for the four time regions I–IV, labelled with timescales 18:00–21:00, 21:00–00:00, 00:00–03:00 and 03:00–06:00 respectively in Figure 12 are consistent with changes in the zonal wind computed using the HWM model.

Conclusion

We have presented the results of the characteristic OI 630.0 nm all-sky imaging observations carried out at low-latitude stations, Kolhapur and Panhala. The main features of present investigation are summarized below:

- The plasma bubbles (depletions) were generally aligned along north-south direction with eastward movement.
- The depletions had varying degrees of depth. The east-west extent of the depletions was found to vary with depletion width. Shallower depletions appeared to be associated with smaller zonal width compared to steeper depletions. A straight-line fit to all the curves (Figure 9) showed that for the OI 630.0 nm images, the degree of depletion ranged between 10 and 25%. These are the typical values computed for the two nights.
- Some of the observed depletions showed westward tilts or structures³⁴. The reason for this tilt is that an eastward neutral wind blowing through a depletion region could polarize the depletion so that it drifted eastward with a velocity less than the ambient $E \times B$ eastward drift. Thus relative to the background ionosphere, the depletions drift eastward as they rise, which accounts for their westward tilt. According to Anderson and Mendillo⁸, these westward tilts are due to the fact that above the F2 peak, the eastward plasma drift set up by the zonal wind decreases with altitude.
- The depletions were normally confined to the time interval between 21:00 to 01:00 IST.
- There were simultaneous depletions observed in all three oxygen emission lines (OI 630, OI 557.7 and OI 777.4 nm) on the ten nights of our observation. The simultaneous depletions for the night of 2 March

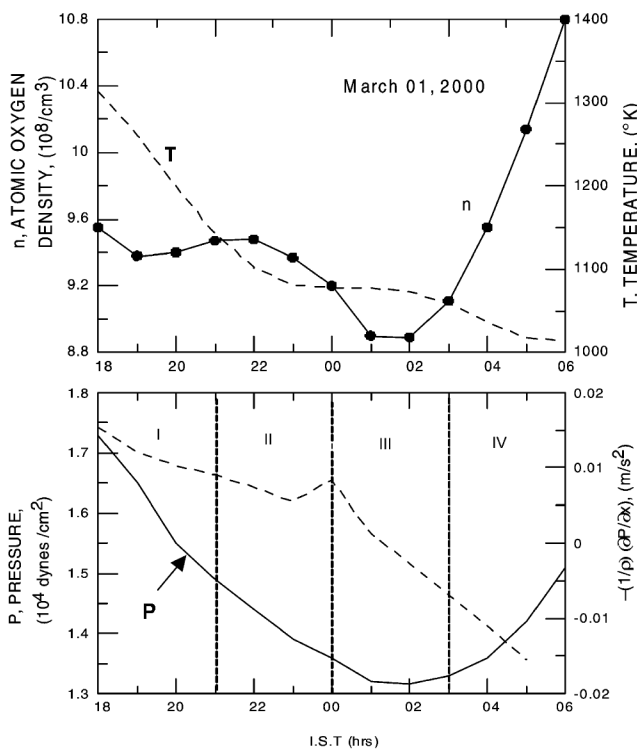


Figure 12. (Upper panel) Night-time variation of neutral oxygen density (n) and temperature and (Lower panel) consequent pressure (P ; in solid line) and zonal driving term $-(1/\rho)(\partial P/\partial x)$; (dotted line) at Kolhapur for the night of 1 March 2000, using the MSIS-E 90 model.

2000 are shown in Figure 5. Depletions observed in OI 777.4 nm mean that the irregularities have reached the peak height of the F2 layer.

- (f) The zonal plasma bubble drift velocities were eastward throughout the night, during all the months studied. The average eastward plasma drift velocity was found to vary between 50 and 260 m/s. The drift speeds were also computed earlier at low-latitude regions using other techniques such as VHF scintillation and radar experiments. As the scale size of the irregularities studied was different in each technique^{11,12,14}, the reported drift velocities varied from about 0 to 289 m/s and 40 to 190 m/s.
- (g) We also observed that the ambient plasma (high-intensity bright region) and the plasma bubbles (low-intensity region) move eastward almost with the same velocity (Figure 8). In the night-time equatorial *F*-region, the eastward neutral wind develops a vertically downward polarization electric field, which drives the plasma eastward. In the absence of drainage of polarization charges, the neutral wind and $E \times B$ plasma drift become almost equal. Under these conditions the background plasma, the neutral wind and plasma bubbles move eastward with the same velocity¹².
- (h) The characteristic variation in zonal component of the neutral wind at night has been well explained in terms of pressure gradient and mass density.

1. Booker, H. G. and Wells, H. W., Scattering of the radio waves by the *F*-region of the ionosphere. *J. Geophys. Res.*, 1938, **43**, 247–256.
2. Rastogi, R. G., On the equatorial spread-*F*. *Proc. Indian Acad. Sci.*, 1978, **87**, 115–131.
3. Rastogi, R. G., On the occurrence of equatorial spread-*F* in the evening hours. *J. Atmos. Sol. Terr. Phys.*, 1986, **48**, 687–693.
4. Abdu, M. A., Equatorial spread-*F* and ionosphere–thermosphere system: A review. *Trends Geophys. Res.*, 1993, **2**, 193–209.
5. Abdu, M. A., Batista, I. S. and Bittercourt, J. A., Some characteristics of spread-*F* at the magnetic equatorial station Fortaleza. *J. Geophys. Res.*, 1981, **86**, 6836–6841.
6. Abdu, M. A., DeMedeiros, R. T. and Nakaymura, Y., Latitudinal and magnetic flux tube extension of the equatorial spread-*F* irregularities. *J. Geophys. Res.*, 1983, **88**, 4861–4868.
7. Basu, S. and Kelly, M. C., A review of recent observations of equatorial scintillation and the relationship to current theories of *F*-region irregularity generation. *Radio Sci.*, 1979, **14**, 471–485.
8. Anderson, D. N. and Mendillo, M., Ionospheric conditions affecting the evolution of equatorial plasma depletions. *Geophys. Res. Lett.*, 1983, **10**, 541–544.
9. Anderson, D. N., Heelis, R. A. and McClure, J. P., Calculated nighttime eastward plasma drift velocities at low-latitudes and their solar cycle dependence. *Ann. Geophys. A*, 1987, **5**, 435–442.
10. McClure, J. P., Hanson, W. B. and Hoffman, J. H., Plasma bubbles and irregularities in the equatorial ionosphere. *J. Geophys. Res.*, 1977, **75**, 7199–7216.
11. Mukherjee, G. K., Studies of equatorial *F*-region depletions and dynamics using multiple wavelength nightglow imaging. *J. Atmos. Sol. Terr. Phys.*, 2003, **65**, 379–390.
12. Basu, S. *et al.*, Scintillations, plasma drifts and neutral winds in the equatorial ionosphere after sunset. *J. Geophys. Res.*, 1996, **101**, 26795–26809.
13. Sahai, Y., Aarons, J., Mendillo, M., Baumgardner, J., Bittercourt, J. A. and Takahashi, H., OI 630 nm imaging observations of equatorial observations of plasma depletions at 16°S dip latitude. *J. Atmos. Terr. Phys.*, 1994, **56**, 1461–1475.
14. Sinha, H. S. S. and Raizada, S., Some new features of ionospheric plasma depletions over the Indian zone using all-sky optical imaging. *Earth Planets Space*, 2000, **52**, 549–559.
15. Weber, E. J., Bachau, J., Eather, R. H. and Mende, S. B., North-south aligned equatorial airglow depletions. *J. Geophys. Res.*, 1978, **83**, 712–716.
16. Weber, E. J., Buchau, J. and Moore, J. G., Airborne studies of equatorial *F*-layer irregularities. *J. Geophys. Res.*, 1980, **85**, 4631–4641.
17. Herrero, F. A., Spencer, N. W. and Mayr, H. G., Thermosphere and *F*-region plasma dynamics in the equatorial region. *Adv. Space Res.*, 1993, **13**, 200–220.
18. Prakash, S., Production of electric field perturbations by gravity wave winds in the *E*-region suitable for initiating equatorial spread-*F*. *J. Geophys. Res.*, 1999, **104**, 10051–10069.
19. Kelley, M. C., *The Earth's Ionosphere*, Academic Press, CA, USA, 1989.
20. Martyn, D. F., The normal *F*-region of the ionosphere. *Proc. IRE*, 1959, **47**, 147–155.
21. Biondi, M. A., Meriwether Jr, J. W., Fejer, B. and Woodman, R., Measurements of the dynamics and coupling of the equatorial thermosphere and *F*-region ionosphere over Peru. *J. Atmos. Terr. Phys.*, 1988, **45**, 697–705.
22. Dungey, J. W., Convective diffusion in the equatorial spread-*F* region. *J. Atmos. Terr. Phys.*, 1956, **9**, 304–310.
23. Hysell, D. L., Kelly, M. C., Swartz, W. and Woodman, R. F., Seeding and layering of equatorial spread *F* by gravitational waves. *J. Geophys. Res.*, 1990, **95**, 1725.
24. Mendillo, M., Baumgardner, J., Xiaoqing, P., Sultan, P. J. and Tsunoda, R., Onset conditions for equatorial spread-*F*. *J. Geophys. Res.*, 1991, **97**, 13865–13876.
25. Mukherjee, G. K., Carlo, L., Mahajan, S. H. and Patil, P. T., First results of all-sky imaging from India. *Earth Planets Space*, 1998, **50**, 119–127.
26. Pimenta, A. A., Bittercourt, J. A., Fagundes, P. R., Sahai, Y., Buriti, R. A., Takahashi, H. and Taylor, M. J., Ionospheric plasma bubble zonal drifts over the tropical region: A study using OI 630 nm emission all-sky images. *J. Atmos. Sol. Terr. Phys.*, 2003, **65**, 1117–1126.
27. Pimenta, A. A., Bittercourt, J. A., Fagundes, P. R., Sahai, Y. and Abalde, J. R., Equatorial *F*-region plasma depletion drifts: Latitudinal and seasonal variations. *J. Ann. Geophys.*, 2003, **21**, 2315–2322.
28. Ryoji, M., *Observations of Gravity Waves in the Mesopause Region by Multicolor Airglow Imaging*, Kyoto University, 2000.
29. Singh, S., Johnson, F. S. and Power, R. A., Gravity wave seeding of equatorial plasma bubbles. *J. Geophys. Res.*, 1997, **102**, 7399–7410.
30. Rishbeth, H., The *F*-layer dynamo. *Planet. Space Sci.*, 1971, **19**, 276–278.
31. Kubota, M., Fukunishi, H. and Okano, S., Characteristics of medium and large-scale TIDs over Japan derived from OI 630 nm night glow observation. *Earth Planets Space*, 2001, **53**, 741–751.
32. Hedin, A. E., Fleming, E. L., Manson, A. H., Tsuda, T., Vial, F., Vincent, R. A., Empirical wind model for the upper, lower and middle atmosphere. *J. Atmos. Sol. Terr. Phys.*, 1996, **58**, 1421–1427.
33. Hedin, A. E., Extension of the MSIS thermosphere model into the middle and lower atmosphere. *J. Geophys. Res.*, 1991, **96**, 1159–1172.
34. Mendillo, M. and Taylor, A., Geometry of depleted plasma regions in the equatorial ionosphere. *J. Geophys. Res.*, 1983, **88**, 5778–5782.

ACKNOWLEDGEMENTS. The nightglow observations at Kolhapur were carried under collaborative research program between IIG, Navi Mumbai and Shivaji University, Kolhapur. Technical support received from Mr P. T. Patil, T.O. IV in Airglow work is gratefully acknowledged.

Received 10 October 2006; revised accepted 1 May 2007